

LES of a high Reynolds number jet for acoustics

C. Bogey* and C. Bailly†

Laboratoire de Mécanique des Fluides et d'Acoustique
Ecole Centrale de Lyon, UMR CNRS 5509
36, av. Guy de Collongue, 69134 Ecully, France
<http://www.lmfa.ec-lyon.fr/autres/CAA/caaweb.html>

Abstract

An isothermal jet with a Mach number of $M = 0.9$ and a high Reynolds number of $Re_D = 4 \times 10^5$ is computed by LES. Both the flow field and the sound field obtained directly from the unsteady compressible simulation are found to be in good agreement with the corresponding measurements of the literature. In particular, the acoustic field shows spectral and two-point properties, as a function of the observation angle, which are characteristic of such a high Reynolds number jet.

1 Introduction

The Direct Noise Computation (DNC) consists in calculating the aerodynamic noise directly by solving the unsteady compressible Navier-Stokes equations,¹ without any acoustic modelling. This methodology has recently been applied to subsonic jets, using Direct Numerical Simulation (DNS),² and using Large Eddy Simulation (LES).³⁻⁷ Unlike DNS where all turbulent scales must be calculated, LES resolves only the scales larger than the mesh grid size. For this, LES is not restricted to low Reynolds numbers, which makes the use of LES especially attractive. In the last two years, LES has been applied to compute the noise radiated by low or moderate Reynolds number jets. For example, the first LES performed by the authors³ to demonstrate the feasibility of the approach for subsonic jet noise involved a jet with a Mach number of $M = u_j/c_a = 0.9$ and a Reynolds number of $Re_D = u_j D/\nu = 6.4 \times 10^4$ (u_j is the jet nozzle exit, c_a the ambient sound speed, D the jet diameter, and ν the molecular viscosity). It is now necessary to deal with higher Reynolds number jets, which are in particular characterized by broadband acoustic spectra⁸ with a peak for a Strouhal number about $St = fD/u_j = 0.8$ for observation angles around 90° .

With this aim in view, the LES of a high Reynolds number is carried out in the present study. The jet is isothermal with $T_j = T_a$ (T_a is the ambient temperature). The Mach number is $M = 0.9$ and the jet diameter is chosen to be $D = 2$ cm yielding a Reynolds number of $Re_D = 4 \times 10^5$. The motivation is to obtain the flow field and the radiated sound field in the same computation, on a mesh grid containing a large part of the acoustic field, and to demonstrate

*CNRS Research Scientist, christophe.bogey@ec-lyon.fr

†Assistant Professor, christophe.bailly@ec-lyon.fr

that both correspond to the considered high Reynolds number. The LES is performed using an in-house LES solver (ALESIA^{3,9}), developed for DNC using accurate, low dispersive and low dissipative numerical schemes, and efficient non-reflecting boundary conditions.

The present paper is organized as follows. The governing equations and the numerical procedure are presented in section 2. The simulation parameters and snapshots of the LES results are shown in section 3. The flow field and the sound field provided directly by LES are then investigated in sections 4 and 5, respectively. Flow and acoustic results are compared to the available measurements of the literature, to determine if they correspond really to the high Reynolds number of the computed jet. Finally, concluding remarks and further works are given in section 6.

2 Governing equations and numerical procedure

2.1 Filtered Navier-Stokes equations

The filtered compressible Navier-Stokes equations are solved. They can be written as¹⁰

$$\frac{\partial \bar{\rho}}{\partial t} + \frac{\partial}{\partial x_j} (\bar{\rho} \tilde{u}_j) = 0 \quad (1)$$

$$\frac{\partial}{\partial t} (\bar{\rho} \tilde{u}_i) + \frac{\partial}{\partial x_j} (\bar{\rho} \tilde{u}_i \tilde{u}_j + \bar{p} \delta_{ij} - \tilde{\tau}_{ij} - \mathcal{T}_{ij}) = 0 \quad (2)$$

$$\frac{\partial}{\partial t} (\bar{\rho} \tilde{e}) + \frac{\partial}{\partial x_j} ((\bar{\rho} \tilde{e} + \bar{p}) \tilde{u}_j - \tilde{\tau}_{ij} \tilde{u}_j + \tilde{q}_j + \mathcal{Q}_j) - \tilde{u}_i \frac{\partial \mathcal{T}_{ij}}{\partial x_j} = 0 \quad (3)$$

where the flow variables ρ , u_i and p are the density, velocity and pressure, and γ is the specific heat ratio. The spatial LES filter associated to the grid, denoted by an overbar, is applied to the density, to the momentum ρu_i and to the pressure. The quantities indicated by a tilde are based on the filtered variables, e.g. the velocity $\tilde{u}_i = \overline{\rho u_i} / \bar{\rho}$ (Favre or density-weighted filtering), and the resolved total energy $\bar{\rho} \tilde{e}$ is given by

$$\bar{\rho} \tilde{e} = \frac{\bar{p}}{\gamma - 1} + \frac{1}{2} \bar{\rho} \tilde{u}_k \tilde{u}_k$$

The resolved viscous stress tensor $\tilde{\tau}_{ij}$ is defined by

$$\tilde{\tau}_{ij} = 2\mu \left(\tilde{S}_{ij} - \frac{1}{3} \tilde{S}_{kk} \delta_{ij} \right) \quad \text{where} \quad \tilde{S}_{ij} = \frac{1}{2} \left(\frac{\partial \tilde{u}_i}{\partial x_j} + \frac{\partial \tilde{u}_j}{\partial x_i} \right)$$

and μ is the molecular dynamic viscosity. In addition, the heat flux \tilde{q}_j is given by:

$$\tilde{q}_j = -\lambda \frac{\partial \tilde{T}}{\partial x_j}$$

where the resolved temperature \tilde{T} is deduced from filtered density and pressure by the equation of state $\bar{p} = \bar{\rho} r \tilde{T}$, and $\lambda = \mu c_p / \sigma$ is the thermal conductivity (σ molecular Prandtl number, c_p specific heat at constant pressure).

Among the different terms resulting from the filtering of the Navier-Stokes equations, the two following ones are classically kept: the subgrid turbulent stress tensor $\mathcal{T}_{ij} = \overline{\rho \tilde{u}_i \tilde{u}_j} - \overline{\rho u_i u_j}$

and the pressure-velocity subgrid term $\mathcal{Q}_j = -(\overline{p\tilde{u}_j} - \overline{p}u_j)/(\gamma - 1)$. The classical modelling of \mathcal{T}_{ij} consists in taking into account the dissipative effects of the unresolved scales through a turbulent viscosity. In the present study at a high Reynolds number, such a subgrid modelling might be too dissipative. For this reason, we set $\mathcal{T}_{ij} = 0$ and $\mathcal{Q}_j = 0$, and a selective filtering, affecting only the high waves numbers, is applied to ensure the dissipation of the subgrid scales. The efficiency of this kind of numerical subgrid modelling will be demonstrated by the good agreement with the experimental data. Further works will still be necessary to study carefully the influence of the different formulations of subgrid modellings on flow and acoustics.

2.2 Numerical algorithm

The numerical algorithm is built up with a thirteen-point stencil finite-difference scheme for the spatial discretization, with a six-stage low storage Runge-Kutta algorithm for the time integration, and with a thirteen-point stencil selective filter to eliminate the grid-to-grid oscillations in order to ensure numerical stability. The numerical schemes¹¹ used in the LES solver are optimized in the Fourier space to be accurate up to four point per wavelength, and to account very properly for the spectral cut-off of the turbulence by the mesh grid. Thus it can be stated with certainty that fluctuations discretized by 4 points per wavelength or more are neither distorted nor dissipated by the numerical procedure. The mesh grid is Cartesian, and slightly non uniform with a typical stretching rate of 2%, in order to use different discretizations in the flow field and in the acoustic far-field while preserving the low dispersive and low dissipative properties of the schemes.

2.3 Boundary conditions

Efficient non-reflective boundary conditions are implemented to minimize the magnitude of the acoustic waves generated when fluctuations leave out the computational domain, and thus to permit the Direct Noise Computation. They combine the use of a far-field formulation¹² of the sound waves in the acoustic far-field, with the application of a sponge zone in the outflow region to dissipate flow fluctuations before they reach the boundary. The sponge zone is based on a grid stretching coming with a Laplacian filtering.¹² Finally, the boundary conditions relies on equations written on the fluctuating quantities alone, and adjustment terms must have been added to impose the values of the mean quantities: outside the flow, mean density and mean pressure are set to the ambient density and pressure, and at the jet inflow, all the mean variables are set to the initial flow values.

3 Simulation parameters and results

3.1 Jet inflow

A circular isothermal jet at flow conditions $M = u_j/c_a = 0.9$ is investigated. This high Mach number is appropriate to keep the computation at an affordable cost, and to make the direct calculation of the acoustic field easier by enhancing the sound pressure levels. It corresponds

also to a value found in a large amount of experimental studies of the literature, providing both aerodynamic results,¹³⁻¹⁶ and acoustic results.^{8,17,18} The jet diameter is chosen as $D = 2$ cm, defining a Reynolds number $\text{Re}_D = 4 \times 10^5$. It must be emphasized that the present Reynolds number is quite high with respect to the range of Reynolds numbers classically considered in LES ($10^3 \leq \text{Re}_D \leq 10^5$).

For high Reynolds numbers $\text{Re}_D \geq 10^5$, the jet exit boundary layers are very thin¹⁹ with a momentum thickness of the order of $10^{-3}D$, and the number of points necessary for its discretization would be exorbitant.²⁰ Therefore in the present LES, the jet inflow conditions have been modeled by imposing mean flow profiles while using an random excitation to seed the turbulence. The inflow longitudinal velocity $u(r)$ is given by the hyperbolic-tangent profile

$$\frac{u(r)}{u_j} = \frac{1}{2} + \frac{1}{2} \tanh\left(\frac{r_0 - r}{2\delta_\theta}\right)$$

where u_j is the inflow centerline velocity, δ_θ the initial momentum thickness of the annular shear layer, and r_0 the jet radius. Pressure is taken as the ambient pressure, radial and azimuthal velocities are set to zero. The density profile is given by the following Crocco-Buseman relation

$$\frac{\rho(r)}{\rho_j} = \left(1 + \frac{\gamma - 1}{2} \text{M}^2 \frac{u(r)}{u_j} \left(1 - \frac{u(r)}{u_j}\right)\right)^{-1}$$

for an isothermal jet. The ratio between the shear-layer momentum thickness and the jet radius is $\delta_\theta/r_0 = 0.05$. This ratio is directly connected to the number of grid points in the jet diameter, and thus to the computational cost, which is clearly limited in 3-D simulations. However its present value is small enough to allow the development of turbulent structures in the shear zone. The profile of the inflow longitudinal velocity is then represented in Figure 1(a).

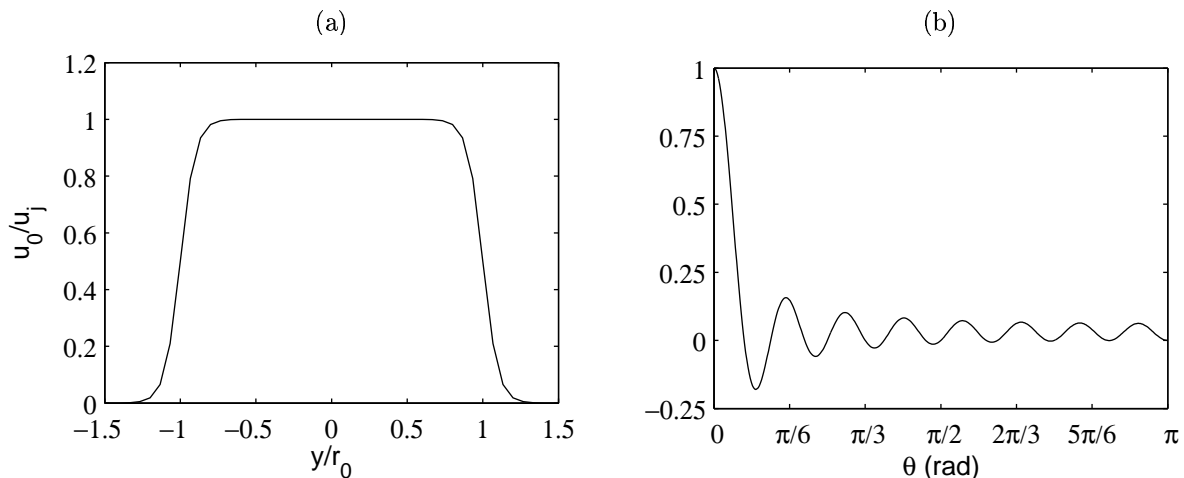


Figure 1: (a) Transverse profile of the inflow velocity u_0/u_j at $x = 0$ and $z = 0$. (b) Azimuthal cross correlation of the velocity disturbances introduced in the inflow shear layers.

To start the turbulent flow development, the jet is forced by adding random velocity fluctuations to the mean profiles, in the shear zones for $x \simeq r_0$. For the noise computation, it is important that this excitation does not radiate noise with a significant magnitude. The excitation fluctuations are therefore solenoidal³ and they are applied only on a few grid points at a

low level. A great care is also taken to be sure that the inflow forcing is random enough not to bias the flow development. The forcing fluctuations are random both in time, and in space as demonstrated by the correlation function of Figure 1(b).

3.2 Numerical specifications

The Cartesian mesh grid is represented in Figure 2, and contains about 12 million points ($255 \times 221 \times 211$). The discretizations in the y and z directions are the same and are symmetrical about the jet axis. Radially, the mesh spacing is uniform for $y \leq 3r_0$ with $\Delta y_0 = r_0/15$. A grid stretching at a rate 2% is then applied to reach well outside the jet $\Delta y = 0.4r_0$, which provides a cut-off Strouhal number of about 2 for the sound field. In the axial direction, the mesh spacing is constant up to $x = 28r_0$ with $\Delta x = 2\Delta y_0$. Then, meshes are stretched to form a sponge zone. The Laplacian filtering used to damp the flow disturbances is applied from $x = 26r_0$ in the flow region only, with a magnitude increasing exponentially as a function of the axial distance.

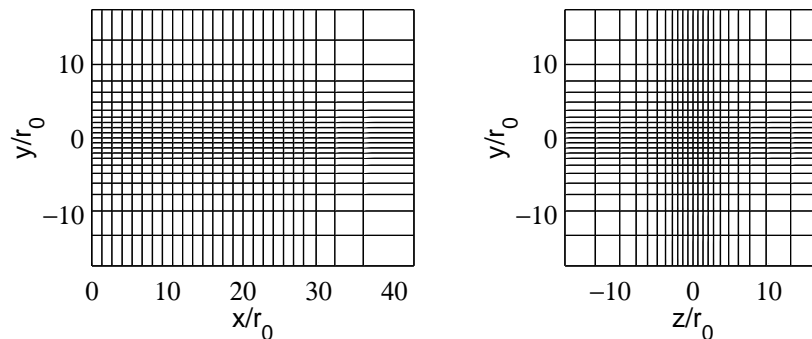


Figure 2: Visualization of the $x - y$ and $y - z$ sections of the mesh grid. Only every tenth line is shown.

The time step is $\Delta t = 0.85\Delta_0/c_0$, and 4×10^4 iterations are performed. The simulation time is $T = 0.067$ s or $2270r_0/c_0$, and corresponds also to the non-dimensional time $Tu_j/D = 1/St = 1010$. The calculations of the mean flow values, of the turbulence intensities and of the acoustic quantities, involve, respectively, the 3.6×10^4 , 2.5×10^4 and 3.3×10^4 final iterations. The sampling time is therefore long enough to achieve statistical convergence for both flow and acoustics. Finally, the computation lasts about 100 hours on a supercomputer Nec SX-5, with an average time of $0.7 \mu\text{s}$ per grid point and per iteration and a CPU speed of 4500 Mflops.

3.3 Instantaneous vorticity and pressure

Longitudinal and transverse sections of the instantaneous LES quantities are displayed in Figure 3, with the vorticity $|\omega|$ in the turbulent flow region and the fluctuating pressure p' outside.

The vorticity field shows a large range of vortical scales, with a fine turbulence which is clearly visible, in accordance with the high Reynolds number. The longitudinal section illustrates the axial flow development from turbulent shear layers to a fully turbulent jet. The shear layers appear to interact in the vicinity of $x = 10r_0$. The length of the potential core is then of about $10r_0$, which is comparable to the values measured on corresponding jets.¹³

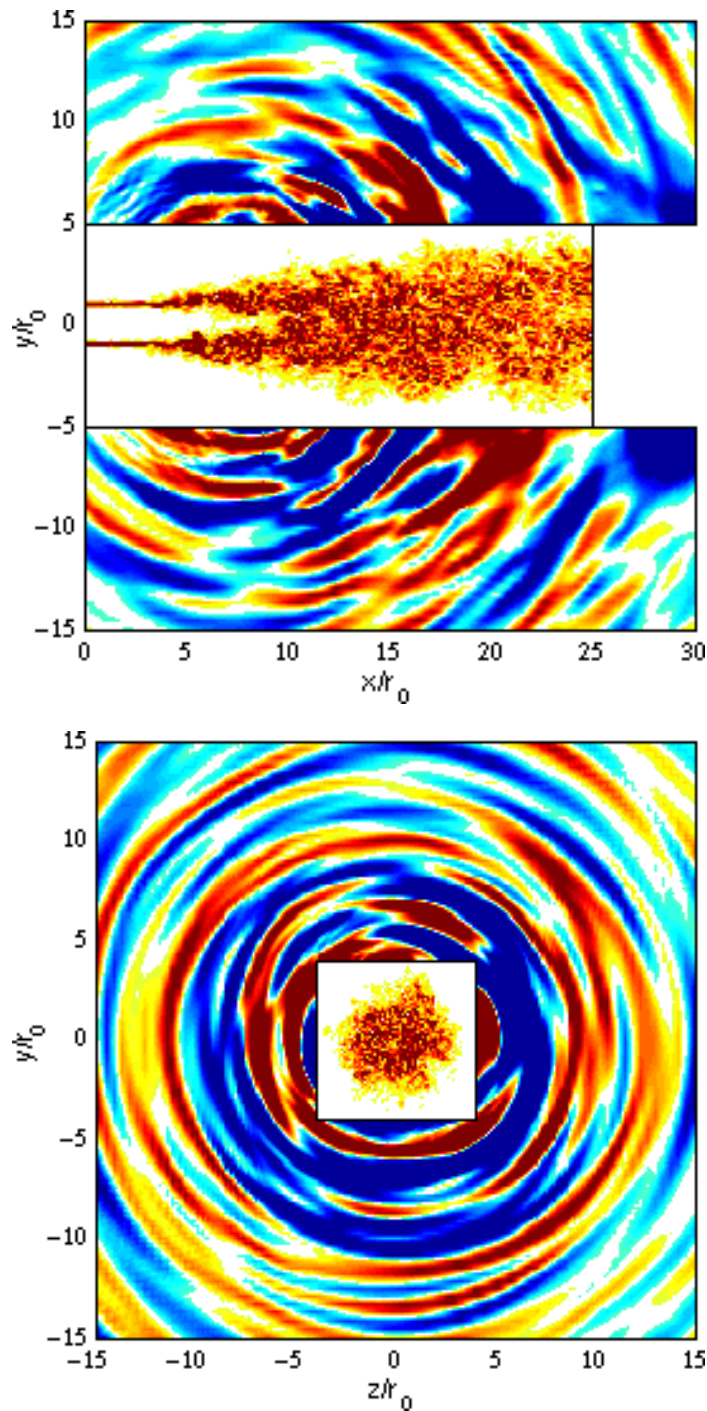


Figure 3: Snapshots of the the vorticity field $|\omega|$ in the flow and of the fluctuating pressure field p' provided directly by LES outside. Top: in the $x - y$ plane at $z = 0$. Bottom: in the $y - z$ plane at $x = 11r_0$. The color scales are defined from -8×10^4 to 8×10^4 s^{-1} for the vorticity and from -70 to 70 Pa for the pressure.

The instantaneous pressure fields demonstrate that the noise generated by the jet is well taken into account by the simulation: it is properly propagated in the acoustic region, and is contaminated neither by the inflow forcing, nor by possible reflections at the boundaries. The longitudinal section shows sound waves originating from a region located in the vicinity of the end of the potential core, in agreement with experimental observations.²¹ The acoustic radiation is also more pronounced in the downstream direction, as expected. The transverse section presents the structure of the sound waves. Waves of partially circular shape are found in the considered section at $x = 11r_0$, but they appear not to be strongly correlated azimuthally. Cross correlations will be given in section 5 to support this observation.

4 Flow field

4.1 Mean flow

Some streamlines originating from points near the mesh boundaries are presented in Figure 4. They illustrate the entrainment of the surrounding fluid in the jet, and demonstrate that the boundary conditions are well appropriate for the incoming of fluid in the computational domain. Fairly parallel to the jet near the inflow, the streamlines are more perpendicular to the flow direction as the axial distance increases and as the jet becomes fully turbulent. This is in good agreement with experimental observations.²²

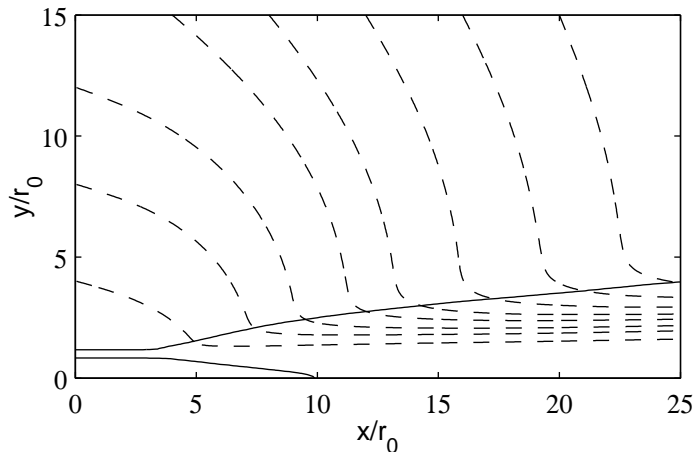


Figure 4: Visualization of the mean velocity field: — iso-contours of the mean longitudinal velocity corresponding to $0.04 \times u_j$ and $0.96 \times u_j$, - - streamlines.

The centerline profile of the mean axial velocity is displayed in Figure 5(a). As expected according to Figure 3, the velocity decay starts for $x \simeq 10r_0$ at the end of the potential core. The decay is in good agreement with the one measured by Lau *et al.*¹³ for a similar jet. A small deceleration of the centerline velocity can also be detected for about $x = 5r_0$. It is interesting to note that this behaviour within the potential core has been observed experimentally.²³

The axial profile of the jet half-width $\delta_{0.5}$ is represented in Figure 5(b). The jet spreads slowly before the end of the potential core, but quite rapidly and apparently linearly after. The evolution of the jet half-width agrees with the measurements conducted by Zaman.²⁴

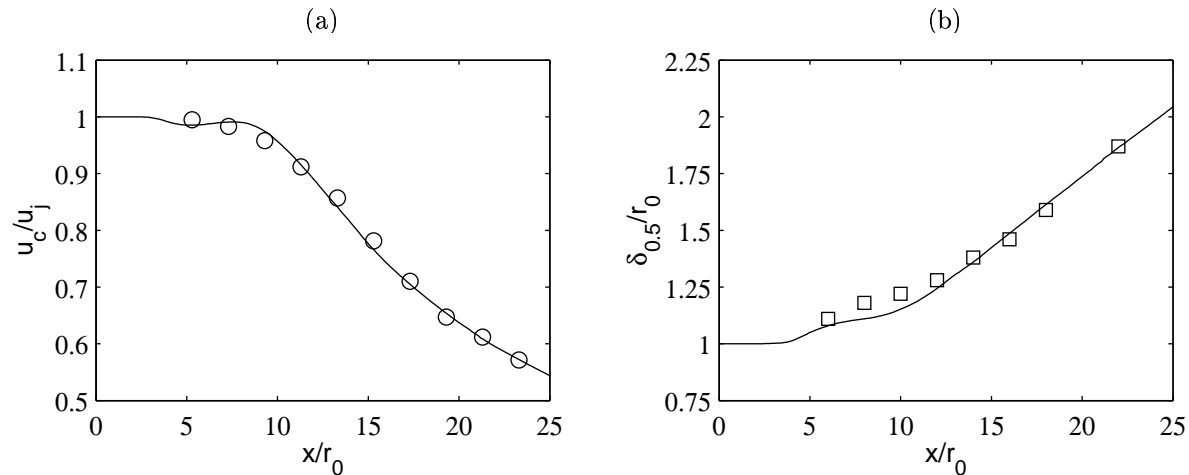


Figure 5: Longitudinal profiles of: (a) the mean centerline velocity u_c/u_j , (b) the jet half-width $\delta_{0.5}/r_0$. Measurements: \circ Lau *et al.*¹³ ($M = 0.9$, $Re_D = 10^6$), \square Zaman²⁴ ($M = 0.5$, $Re_D = 3 \times 10^5$), both are spatially shifted to match the locations of the end of the potential core.

Moreover, no velocity decay constant and no spreading rate are provided since experimental values are calculated very far downstream from the jet exit, typically $x > 60r_0$,²⁵ and the comparisons would not be relevant.

4.2 Turbulence intensities

The centerline profile of the turbulent axial velocity $\langle u'u' \rangle^{1/2}/u_j$ is plotted in Figure 6. The profile reaches a peak for about $x = 14r_0$, slightly after the end of the potential core, in the transition region where the turbulent shear layers merge. The increase and the peak value of the turbulent velocity are compared successfully to data provided by PIV measurements on $M=0.9$, similar Reynolds number jets. These comparisons support that the jet transition is well taken into account by the LES. This is of importance since the end of the potential core is known as a region of significant noise generation.

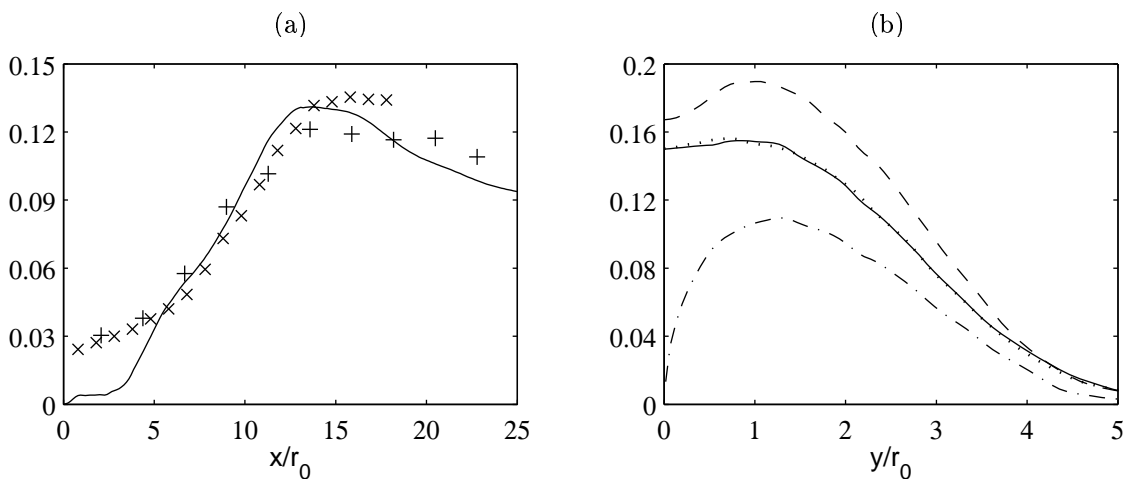


Figure 6: (a) Centerline profiles of the turbulent axial velocity $\langle u'u' \rangle^{1/2}/u_j$. Measurements: \times Jordan *et al.*¹⁵ ($M = 0.9$, $Re_D = 10^6$), $+$ Arakeri *et al.*¹⁶ ($M = 0.9$, $Re_D = 5 \times 10^5$), both are spatially shifted to match the locations of the end of the potential core. (b) Radial profiles at $x = 20r_0$ of the turbulence intensities: $---$ $\langle u'u' \rangle^{1/2}/u_c$, $—$ $\langle v'v' \rangle^{1/2}/u_c$, \cdots $\langle w'w' \rangle^{1/2}/u_c$, $- \cdot - \cdot$ $\langle u'v' \rangle^{1/2}/u_c$.

To study more particularly the turbulent region, the turbulence intensities calculated using the local centerline velocity u_c are investigated. Their radial profiles are represented in Figure 6 for $x = 20r_0$. It is observed that their values on the jet axis at this axial location are lower than the values measured in the jet self-preserving region with, for example, $\langle u'u' \rangle^{1/2}/u_c \simeq 0.25$ in the recent literature.^{26,27} This can be certainly due to the fact that, in a high Reynolds number jet, the turbulence intensities become self-similar only around 100 radii downstream the nozzle.²⁵ Therefore the computational domain is too small to reach the self-similarity zone. However, their relative shapes agree well with measurements.^{26,27}

5 Acoustic field

5.1 Sound pressure spectra

Sound spectra are calculated from the pressure signals recorded at two observation points at $x = 29r_0$ and $r = 12r_0$, and at $x = 11r_0$ and $r = 15r_0$. These points are chosen to describe angles of about $\theta = 30^\circ$ and $\theta = 90^\circ$ from the jet axis, with an origin taken at the end of the potential core where the dominant sound sources are likely to be located. The spectra are shown in Figure 7 and they appear basically different. The downstream spectrum is dominated by a low-frequency component with a strong peak for a Strouhal number $St \simeq 0.3$, whereas the upstream spectrum is more broadband with a maximum observed for $St \simeq 0.7$. This modification of spectra as a function of the observation angle is in good agreement with the measurements of the sound radiation of high Reynolds number jets.⁸ The pressure spectrum for $\theta = 90^\circ$ corresponds well to the nominal Reynolds number of the simulated jet, and this is of importance with the aim of demonstrating the feasibility of computing high Reynolds number flows by LES.

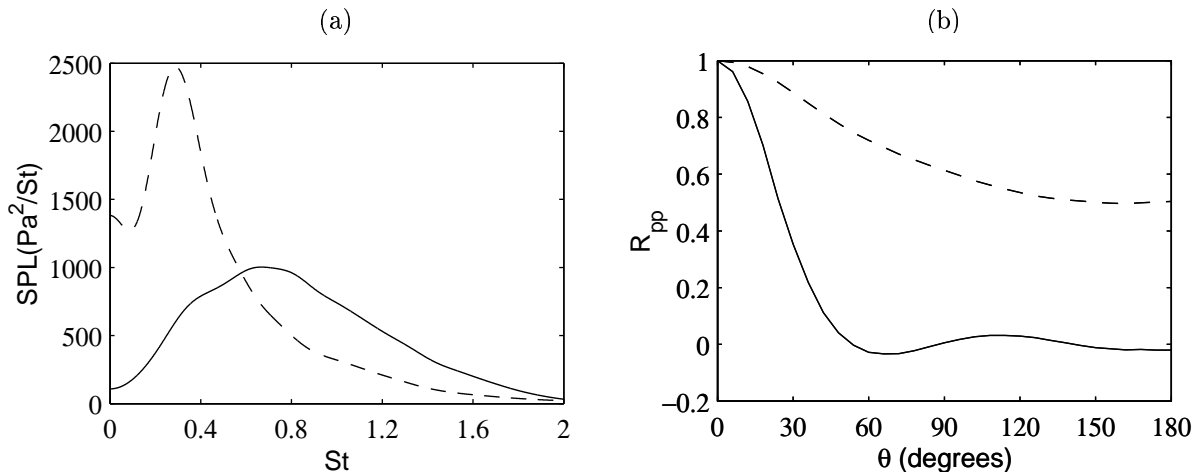


Figure 7: (a) Sound pressure spectra as a function of Strouhal number $St = fD/u_j$ and (b) azimuthal cross correlation of the fluctuating pressure, for — $x = 29r_0$ and $r = 15r_0$, - - - $x = 11r_0$ and $r = 12r_0$, i.e. for angles from the jet axis of about $\theta \simeq 90^\circ$ and of $\theta \simeq 30^\circ$, respectively.

5.2 Azimuthal cross correlations

To more characterize the two kinds of sound radiations found for $\theta = 30^\circ$ and $\theta = 90^\circ$,

the azimuthal cross correlations of the fluctuating pressure are studied. They are displayed in Figure 7(b). As for the sound spectra, the correlation functions differ greatly. For an observation angle of $\theta = 90^\circ$, the correlation level is high, with still $R_{pp} \simeq 0.5$ for two points symmetrically located about the jet axis. However for $\theta = 90^\circ$ the correlation decreases very rapidly and the sound field is only correlated over a range of about 30 degrees. This behaviour is in accordance with experimental observations.²⁸ It supports the presence of two noise mechanisms in the jet: a first one associated to low frequencies within the jet which is likely to be found at the end of the potential core,³ and a second one associated to high frequencies of the turbulent scales and particularly of the mixing zones.

5.3 Sound pressure levels

Figure 8 displays the contours of the overall sound pressure levels computed on the whole computational domain. This shows the strong directivity of the jet noise in the jet axis direction. To the authors' knowledge, there are no data in the literature of the near-field sound pressure levels of a Mach 0.9 jet to compare with the LES results. Moreover it might be hazardous to apply the $1/r$ decay law to compute the far-field sound directivity, since this method requires a large distance to the sound sources.

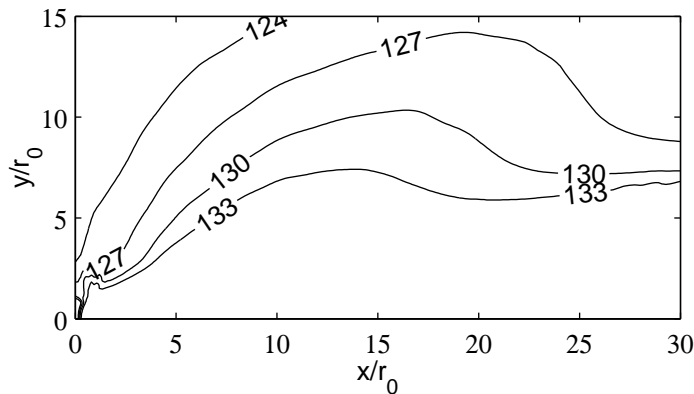


Figure 8: Contours of the overall sound pressure levels in dB.

In the present study, to give a simple comparison of the LES sound pressure levels with the measurements, we consider only the sound radiation at about 30° from the jet axis. The sound level for the point $x = 29r_0$ and $y = 12r_0$ (125 dB) is extrapolated to a distance of 60 radii of the source region assumed to be located at the end of the potential core³ at $x = 10r_0$ using the $1/r$ decay law of the acoustic waves. The computed level is 116.5 dB, in agreement with well-known experimental data (Lush⁸: 115 dB, Mollo-Christensen¹⁷: 116.3 dB, Tanna¹⁸: 115.5 dB).

6 Concluding remarks

A circular isothermal jet with a Mach number $M = 0.9$ and a Reynolds number $Re_D = 4 \times 10^5$ is computed by LES using accurate numerical schemes to determine directly its radiated sound field. Both the flow field and the sound pressure field are in good agreement with correspond-

ing experimental data. These results demonstrate that the effective Reynolds number of the simulated jet is Re_D as expected. This is particularly supported by the behaviour of the sound spectra with a peak moving to higher frequencies as the observation angle increases and by the typical broad shape of the spectrum for $\theta = 90^\circ$.

The present LES data can be used as a reference solution to investigate noise mechanisms, or to study the effects of the different subgrid modelling proposed in the literature on the jet development and on its radiated sound. Other parameters such as the shear-layer momentum thickness should also be the subject of an investigation, to understand clearly what must be done to perform LES of high Reynolds number jets with a full confidence.

Acknowledgments

This work is supported by the EU Research programme JEAN (Jet Exhaust Aerodynamics and Noise) (Contract No. G4RD-CT-2000-00313). Computing time is supplied by the Institut du Développement et des Ressources en Informatique Scientifique (IDRIS - CNRS).

References

- ¹TAM, C.K.W., 1995, Computational aeroacoustics: issues and methods, *AIAA Journal*, **33**(10), 1788-1796.
- ²FREUND, J.B., 2001, Noise sources in a low-Reynolds-number turbulent jet at Mach 0.9, *J. Fluid Mech.*, **438**, 277-305.
- ³BOGEY, C., BAILLY, C. & JUVÉ, D., 2002, Noise investigation of a high subsonic, moderate Reynolds number jet using a compressible LES, to appear in *Theoret. Comput. Fluid Dynamics*. See also AIAA Paper 2000-2009
- ⁴ZHAO, W., FRANKEL, S.H. & MONGEAU, L., 2000, Large eddy simulation of sound radiation from a subsonic turbulent jet, AIAA Paper 2000-2078.
- ⁵CONSTANTINESCU, G.S. & LELE, S., 2001, Large eddy simulation of a near sonic turbulent jet and its radiated noise, AIAA Paper 2001-0376.
- ⁶UZUN, A., BLAISDELL, G.A. & LYRINTZIS, A.S., 2002, Recent progress towards a Large Eddy Simulation code for jet aeroacoustics, AIAA Paper 2002-2598.
- ⁷LUPOGLAZOFF, N., BIANCHERIN, A., VUILLOT, F. & RAHIER, G., 2002, Comprehensive 3D unsteady simulations of subsonic and supersonic hot jet flow-fields, AIAA Papers 2002-2599 and 2002-2600.
- ⁸LUSH, P.A., 1971, Measurements of subsonic jet noise and comparison with theory, *J. Fluid Mech.*, **46**(3), 477-500.
- ⁹BOGEY, C., BAILLY, C. & JUVÉ, D., 2000, Numerical simulation of the sound generated by vortex pairing in a mixing layer, *AIAA Journal*, **38**(12), 2210-2218.
- ¹⁰VREMAN, B., GEURTS, B. & KUERTEN, H., 1995, Subgrid-modelling in LES of compressible flow, *Applied Scientific Research*, **54**, 191-203.
- ¹¹BOGEY, C. & BAILLY, C., 2002, A family of low dispersive and low dissipative explicit schemes for computing the aerodynamic noise, AIAA Paper 2002-2509.
- ¹²BOGEY, C. & BAILLY, C., 2002, Three-dimensional non reflective boundary conditions for acoustic simulations: far-field formulation and validation test cases, *Acta Acustica*, **88**(4), 463-471.

- ¹³LAU, J.C., MORRIS, P.J. & FISHER, M.J., 1979, Measurements in subsonic and supersonic free jets using a laser velocimeter, *J. Fluid Mech.*, **93**(1), 1-27.
- ¹⁴SIMONICH, J.C., NARAYANAN, S., BARBER, T.J. & NISHIMURA, M., 2001, Aeroacoustic characterization, noise reduction, and dimensional scaling effects of high subsonic jets, *AIAA Journal*, **39**(11), 2062-2069.
- ¹⁵JORDAN, P., GERVAIS, Y., VALIÈRE, J.-C. & FOULON, H., 2002, PIV measurements of a Mach 0.9 jet, *personnal communication*.
- ¹⁶ARAKERI, V.H., KROTHAPALLI, A., SIDDAVARAM, V., ALKISLAR, M.B. & LOURENCO, L., 2002, Turbulence suppression in the noise producing region of a Mach=0.9 jet, AIAA Paper 2002-2523.
- ¹⁷MOLLO-CHRISTENSEN, E., KOLPIN, M.A. & MARTUCELLI, J.R., 1964, Experiments on jet flows and jet noise far-field spectra and directivity patterns, *J. Fluid Mech.*, **18**, 285-301.
- ¹⁸TANNA, H.K., 1977, An experimental study of jet noise. Part I: Turbulent mixing noise. *J. Sound Vib.*, **50**(3), 405-428.
- ¹⁹ZAMAN K.B.M.Q., 1985, Far-field noise of a subsonic jet under controlled excitation, *J. Fluid Mech.*, **152**, 83-111.
- ²⁰FREUND, J.B. & LELE, S.K., 2001, in High Speed Jet Flows, Editors: G. Raman, D. McLaughlin, P. Morris, Taylor Francis.
- ²¹JUVÉ, D., SUNYACH, M. & COMTE-BELLOT, G., 1980, Intermittency of the noise emission in subsonic cold jets, *J. Sound Vib.*, **71**(3), 319-332.
- ²²RICOU, F.P. & SPALDING, D.B., 1961, Measurements of entrainment by axisymmetrical turbulent jets, *J. Fluid Mech.*, **11**, 21-32.
- ²³ISLAM, M.T. & ALI, M.A.T., 1997, Mean velocity and static pressure distributions of a circular jet, *AIAA Journal*, **35**(1), 196-197.
- ²⁴ZAMAN, K.B.M.Q., 1986, Flow field and near and far sound field of a subsonic jet, *J. Sound Vib.*, **106**(1), 1-16.
- ²⁵WYGNANSKI, I. & FIEDLER, H., 1969, Some measurements in the self-preserving jet, *J. Fluid Mech.*, **38**(3), 577-612.
- ²⁶PANCHAPAKESAN, N.R. & LUMLEY, J.L., 1993, Turbulence measurements in axisymmetric jets of air and helium. Part I. Air jet. *J. Fluid Mech.*, **246**, 197-223.
- ²⁷HUSSEIN, H.J., CAPP, S.P. & GEORGE, W.K., 1994, Velocity measurements in a high-Reynolds-number, momentum-conserving, axisymmetric, turbulent jet, *J. Fluid Mech.*, **258**, 31-75.
- ²⁸JUVÉ, D. & SUNYACH, M. , 1981, Near and far field azimuthal correlations for excited jets, AIAA Paper 81-2011.